ANNUAL REVIEWS

Annual Review of Condensed Matter Physics

Creep Motion of Elastic Interfaces Driven in a Disordered Landscape

Ezequiel E. Ferrero,[1] Laura Foini,[2] Thierry Giamarchi,[3] Alejandro B. Kolton,[4] and Alberto Rosso[5]

[1]Instituto de Nanociencia y Nanotecnología, Centro Atómico Bariloche, CNEA–CONICET, R8402AGP San Carlos de Bariloche, Río Negro, Argentina

[2]IPhT, CNRS, CEA, Université Paris-Saclay, 91191 Gif-sur-Yvette, France

[3]Department of Quantum Matter Physics, University of Geneva, CH-1211 Geneva, Switzerland

[4]Instituto Balseiro, Centro Atómico Bariloche, CNEA–CONICET–UNCUYO, R8402AGP San Carlos de Bariloche, Río Negro, Argentina

[5]LPTMS, CNRS, Univ. Paris-Sud, Université Paris-Saclay, 91405 Orsay, France; email: alberto.rosso@u-psud.fr

Annu. Rev. Condens. Matter Phys. 2021. 12:111–34

The *Annual Review of Condensed Matter Physics* is online at conmatphys.annualreviews.org

https://doi.org/10.1146/annurev-conmatphys-031119-050725

Keywords

domain walls, depinning, disordered elastic systems, avalanches, activated motion

Abstract

The thermally activated creep motion of an elastic interface weakly driven on a disordered landscape is one of the best examples of glassy universal dynamics. Its understanding has evolved over the past 30 years thanks to a fruitful interplay among elegant scaling arguments, sophisticated analytical calculations, efficient optimization algorithms, and creative experiments. In this article, starting from the pioneer arguments, we review the main theoretical and experimental results that lead to the current physical picture of the creep regime. In particular, we discuss recent works unveiling the collective nature of such ultraslow motion in terms of elementary activated events. We show that these events control the mean velocity of the interface and cluster into "creep avalanches" statistically similar to the deterministic avalanches observed at the depinning critical threshold. The associated spatiotemporal patterns of activated events have been recently observed in experiments with magnetic domain walls. The emergent physical picture is expected to be relevant for a large family of disordered systems presenting thermally activated dynamics.

1. INTRODUCTION

Our understanding of physics is largely based on idealized problems, the famous "spherical cows." Yet, the beauty of nature makes use of vast complexity. It is well known nowadays that the presence of impurities and defects messing up those rounded mammals leads to new emerging physical behavior that is not observed in the idealized disorder-free problems. For example, the equilibration time of glasses becomes so large that the result is experimentally inaccessible. Such systems avoid crystallization and basically live forever out of equilibrium (1, 2). Dirty metals display localization and metal insulator transitions, which is unseen in perfect crystals (3, 4). Systems of a broadly diverse nature show intermittent dynamics induced by the presence of disorder (5). Strained amorphous materials (6–8), fracture fronts (9–11), magnetic (12, 13) and ferroelectric domain walls (14, 15), and liquid contacts lines (16, 17) all share a common phenomenology: When the applied drive is just enough to induce motion, most of the system remains pinned but large regions move collectively at high velocity. These reorganizations are called avalanches. Their location is typically unpredictable, and their size distributions display scale-free statistics. Given the ubiquity of this stick–slip behavior, the study of avalanches has occupied a central scene in nonequilibrium statistical physics, as can be seen in the large literature of sandpile models (18), directed percolation, and cellular automata (19).

The depinning of an elastic interface moving in a disordered medium (20–25) is one of the paradigmatic examples in which avalanches are well understood, thanks to the analogy with standard equilibrium-critical phenomena (22, 26). When the interface is driven at the force, f, two phases are generically observed: For $f < f_c$, the interface is pinned at zero temperature and motion is observed only during a transient time; for $f > f_c$, the line moves with a finite steady velocity. At f_c, the system displays a dynamical phase transition and the diverging size of avalanches is the outcome of the presence of critical correlations. Below and above f_c, the avalanches display a finite cutoff that diverges approaching f_c. We presently know the statistics of avalanche sizes (27) and durations (28) and their characteristic shape (29, 30). An important observation is that subsequent depinning avalanches are uncorrelated in space and time at variance with the avalanche behavior observed in many systems in which a main shock is at the origin of a cascade of aftershocks. The so-called Omori law and productivity law, central in the geophysics of earthquakes (31), are not present at the depinning transition.[1] Namely all the experimental observations of depinning avalanches temporally correlated were shown to be related to a finite detection threshold, created by the limited sensitivity of the measurement apparatus (34).

Nonetheless, genuine aftershocks could be experimentally observed far from the depinning transition in the so-called creep regime. This regime, which describes the motion of magnetic domain walls at finite (e.g., room) temperature and low applied fields, corresponds to an interface pulled by a small force ($f \ll f_c$) at finite temperature (24, 25, 35). The collective dynamics observed in this case is qualitatively different from that at the critical threshold. In both regimes, the dynamics is collective and involves large-scale reorganizations. But from the more recent results, creep avalanches display complex spatiotemporal patterns similar to those observed in earthquakes.

In this article, we review the main arguments and results of the past thirty years about creep, paying particular attention to the recent progress. The article is organized as follows. In Section 2, we introduce the model, present the dynamical regimes at zero temperature, and discuss the different universality classes. In Section 3, we provide the scaling arguments leading to the creep law, namely the behavior of the steady velocity as a function of the applied force at finite temperature.

[1] However, depinning-inspired models have been adapted to produce aftershocks by adding terms of slow relaxation or memory (32, 33).

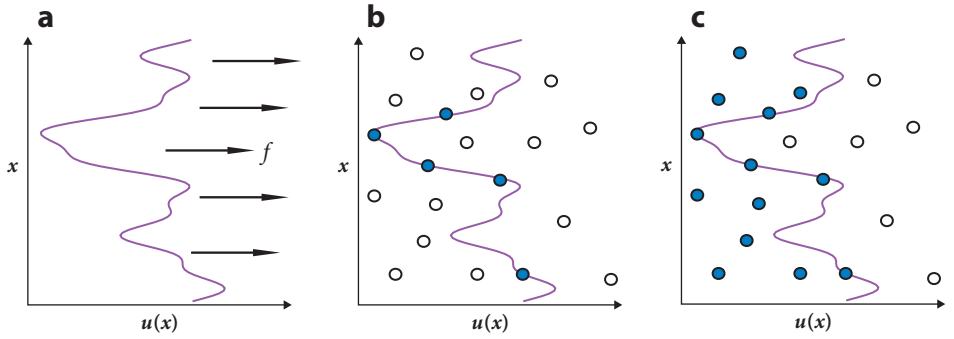

Figure 1

(*a*) Sketch of the interface pulled by an external force *f*. The filled circles are the impurities that contribute to the pinning energy of the interface. In the random bond case (*b*), only neighboring impurities contribute, whereas in the random field case (*c*) all the impurities on the left side of the interface contribute.

The numerical methods are discussed in Section 4. The more recent results valid in the limit of vanishing temperature are presented in Section 5. In Section 6, we review the creep experiments on domain wall dynamics. Conclusions and perspectives are given in Section 7.

2. DYNAMICAL PHASE DIAGRAM AT ZERO TEMPERATURE

We consider a d-dimensional interface in a $d + 1$ disordered medium. For simplicity, we assume that the local displacement at any time t is described by a single valued function $u(x, t)$ (see **Figure 1*a***) and that the dynamics is overdamped. At zero temperature, the equation of motion of the elastic manifold is written as

$$\gamma \partial_t u(x,t) = c\nabla^2 u(x,t) + f + F_{\rm p}(x,u), \qquad 1.$$

where $c\nabla^2 u(x, t)$ describes the elastic force due to the surface tension, f is the external pulling force, and γ is the microscopic friction. The fluctuations induced by impurities are encoded in the quenched stochastic term $F_{\rm p} = -\partial_u V_{\rm p}(x, u)$, where the energy potential $V_{\rm p}(x, u)$ describes the coupling between the manifold and the impurities.

For simplicity, we assume the absence of correlations along the x direction,[2] whereas the correlations of $V_{\rm p}(x, u)$ along the u direction usually belong to one of two universality classes: (*a*) In the random bond (RB) class, the impurities affect, in a symmetric way, the phases on each side of the interface. They thus simply locally attract or repel the interface (see **Figure 1*b***). In this case, the pinning potential and the pinning force are both short-ranged correlated. (*b*) The random field (RF) class describes a disorder coupling in a different way in the two phases around the interface. Thus, the pinning energies are affected by the impurities inside the entire region delimited by the interface (see **Figure 1*c***). Then $F_{\rm p}$ displays short-range correlations while the pinning potential $V_{\rm p}(x, u)$ displays long-range correlations $\overline{[V_{\rm p}(x,u) - V_{\rm p}(x',u')]^2} \propto \delta(x - x')|u - u'|$. Here, the overline denotes an average over disorder realizations.

Equation 1, the so-called quenched Edwards–Wilkinson (qEW) equation, is a coarse-grained minimal model governing the dynamics of the interface, at zero temperature for the moment, at large scales (22, 25, 26). It is a nonlinear equation in u that has been extensively studied by

[2] See Reference 36 for a discussion of the correlated disorder case.

numerical simulation (37), functional renormalization group (FRG) techniques (21, 38, 39), and exact mean-field solutions (40–42). For the case of a contact line of a liquid meniscus (43) as well as the crack front of a brittle material (44), the local elastic force is replaced by a long-range one:

$$c\nabla^2 u \rightarrow c \int \frac{[u(x',t)-u(x,t)]}{|x'-x|^{\alpha+d}} \mathrm{d}^d x', \qquad 2.$$

with $\alpha = 1$ and $d = 1$. The qualitative phenomenology of this generalized long-range model is similar to the qEW, but the universal properties (as critical exponents and scaling functions) are different. However, for $\alpha \geq 2$, one recovers the short-range universality class (45).

The solution of this class of equations shows a behavior reminiscent of second-order phase transitions with the velocity playing the role of the order parameter and the force acting as the control parameter. In particular, the steady velocity is zero below a critical depinning threshold f_c, and it acquires a finite value only above that threshold. The velocity vanishes continuously at the critical force as $v \simeq (f - f_c)^\beta$. At the depinning, the interface appears rough with a width of

$$w^2(L) = \frac{1}{L}\int_0^L u^2(x)\mathrm{d}x - \left[\frac{1}{L}\int_0^L u(x)\mathrm{d}x\right]^2 \qquad 3.$$

that grows as $L^{2\zeta_{\mathrm{dep}}}$, with L being the size of the system and ζ the roughness exponent. Both β and ζ_{dep} are universal depinning exponents depending on the dimension d of the interface and on the range α of the elastic force; but interestingly, these values do not depend on the disorder type (20, 46). Slightly above f_c, the dynamics of a point of the interface is highly intermittent: For long times, the point is stuck with a vanishing velocity (much smaller than the average value v) and suddenly starts to move with a high velocity. In second-order phase transitions at thermodynamic equilibrium, the universality arises from the existence of a correlation length that diverges when the transition is approaching the critical threshold. For depinning, the system is out of equilibrium, but the presence of large spatial correlations is manifested by the collective nature of this intermittent dynamics: At a given time, though many pieces of the interface are at rest, large and spatially connected portions move fast and coherently.

The presence of large correlations can be detected using a quasistatic protocol below (but close to) f_c. This is shown in **Figure 2*a***, where an interface is at rest at a force f. Upon infinitesimally increasing the force $f \rightarrow f + \delta f$, an avalanche takes place: A large portion of the interface advances a finite amount while elsewhere only readjusts infinitesimally ($\propto \delta f$). The avalanche locations cannot be predicted, and their sizes (the areas spanned between two consecutive metastable states) present scale-free statistics:

$$P(S) = S^{-\tau_{\mathrm{dep}}} g(S/S_c). \qquad 4.$$

The Gutenberg–Richter exponent τ is universal, as are β and ζ_{dep}; $g(x)$ is a function that decays fast for $x \geq 1$ and is constant for $x < 1$. The characteristic size of the maximal avalanche increases when $f \rightarrow f_c^-$. In practice, S_c is the clear manifestation of the divergent correlation length $\xi \simeq |f - f_c|^{-\nu_{\mathrm{dep}}}$, and one expects $S_c \simeq \xi^{d+\zeta_{\mathrm{dep}}} \simeq |f - f_c|^{-\nu_{\mathrm{dep}}(d+\zeta_{\mathrm{dep}})}$. Many works describe the dynamics inside an avalanche (28, 33, 34, 47, 48): Typically the instability starts well localized at a given point and spreads in space over a distance $x(t) \simeq t^{1/z}$ up to a time $t_c \simeq \xi^z$. In **Table 1**, we show the relevant depinning exponents, their definition, and their mean-field and numerically known finite-dimension values. For the qEW equation (Equation 1), it has been proven that there are only two independent exponents, e.g., ζ_{dep} and z, and the other exponents can be computed by nontrivial scaling relations (see **Table 1**). Note that these relations are valid in low dimensions, and for $d \geq 2\alpha$ the values of the exponents saturate at their mean-field values.

The physics is very different in the limits of very small or very high forces. The interface is at equilibrium in the ground state at $f = 0$, its roughness is characterized by a very different (smaller)

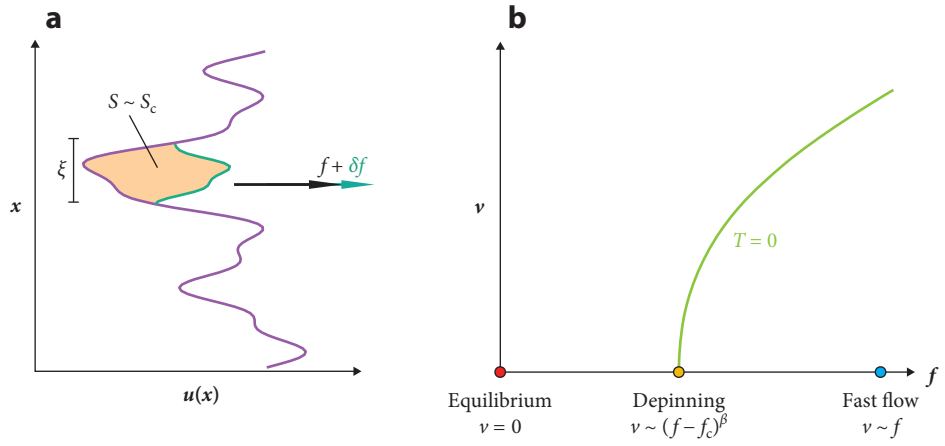

Figure 2

(*a*) Sketch of an avalanche below f_c: The applied force f is increased infinitesimally and a finite portion of the interface is destabilized. The size S of the avalanche corresponds to the spanned area. (*b*) Dynamical phase diagram at zero temperature. At $f = f_c$, the velocity and the shape of the interface have a universal scaling behavior; the dynamics is characterized by large and scale free avalanches. At $f = 0$, the interface is in the ground state with a different roughness exponent, which depends on the correlation of the disorder (random bond or random field). At very large force, the interface flows with a velocity that grows linearly with the force, and the quenched disorder acts as a thermal noise.

roughness exponent, and the nature of the disorder matters: RF interfaces are rougher than RB interfaces. The ground-state energy is an extensive quantity (grows as L^d), but its sample-to-sample fluctuations scale as L^{θ}. In **Table 2**, we show the relevant equilibrium exponents and their mean-field and finite dimension values for RB disorder. For finite dimensions, the energy exponent θ obeys the scaling relation $\theta = 2\zeta_{eq} + d - \alpha$. This relation is a consequence of the statistical tilt symmetry of the model, which assures that the elastic constant c is not renormalized. By contrast, assuming that in equilibrium elastic and disorder energy scale in the same way, one has from

$$E_{el}[u] = \frac{c}{2} \int \frac{[u(x',t) - u(x,t)]^2}{|x' - x|^{\alpha+d}} \mathrm{d}^d x \mathrm{d}^d x' \qquad 5.$$

Table 1 Depinning exponents: mean-field and finite dimension[a]

Depinning exponent	Observable	Mean field $d \geq 2\alpha$	$d = 1 \quad \alpha = 2$	$d = 1 \quad \alpha = 1$	$d = 2 \quad \alpha = 2$
z	$t(L) \sim L^z$	α	1.433	0.77	1.56
ζ_{dep}	$u(x) \sim x^{\zeta_{dep}}$, $w^2 \sim L^{2\zeta_{dep}}$	0	1.250	0.39	0.75
τ_{dep}	$P(S) \sim S^{-\tau_{dep}}$	3/2	$\tau_{dep} = 2 - \alpha/(d + \zeta_{dep})$		
ν_{dep}	$\xi \sim \lvert f - f_c \rvert^{-\nu_{dep}}$	α^{-1}	$\nu_{dep} = 1/(\alpha - \zeta_{dep})$		
β	$v \sim \lvert f - f_c \rvert^{\beta}$	1	$\beta = \nu_{dep}(z - \zeta_{dep})$		

[a]Mean field is valid for $d \geq 2\alpha$, where d is the dimension of the interface and α is the exponent that controls the range of the elastic interactions (Equation 2). In finite dimensions depinning exponents are known numerically and are identical for random bond and random field disorder. The exponent β controls the critical behavior of the velocity-force characteristics close to the transition, and ν_{dep} rules the divergence of the associated correlation length (typical linear extension of avalanches). The dynamical exponent z controls both the spread $x(t)$ of correlations in a developing avalanche and the geometrical equilibration time $t(L)$. The roughness exponent ζ_{dep} governs the width w^2 (Equation 3) and the wandering $u(x)$ of the critical interface configuration. τ_{dep} rules the power-law distribution of avalanche sizes. The displayed numerical values for ζ_{dep} are taken from Reference 49 for $\alpha = 1$ and References 37 and 50 for $\alpha = 2$. Those of z are taken from the following: Reference 37 for $\alpha = 2$, $d = 1$; Reference 51 for $\alpha = 1$, $d = 1$; and Reference 52 for $\alpha = 2$, $d = 2$.

Table 2 Equilibrium exponents with random bond disorder: mean-field and finite dimension[a]

Equilibrium exponent	Observable	Mean field $d \geq 2\alpha$	$d=1$ $\alpha=2$	$d=1$ $\alpha=1$	$d=2$ $\alpha=2$
θ	$E(L) \sim L^{\theta}$	$d/2$	1/3	$\simeq$0.2	$\simeq$0.84
ζ_{eq}	$u(x) \sim x^{\zeta_{eq}}$, $w^2 \sim L^{2\zeta_{eq}}$	0	2/3	$\simeq$0.2	$\simeq$0.41
τ_{eq}	$P(S) \sim S^{-\tau_{eq}}$	3/2	$\tau_{eq} = 2 - \alpha/(d+\zeta_{eq})$		
ν_{eq}	$\xi \sim f^{-\nu_{eq}}$	α^{-1}	$\nu_{eq} = 1/(\alpha - \zeta_{eq})$		

[a]Mean field is valid for $d \geq 2\alpha$, where d is the dimension of the interface and α is the exponent that controls the range of the elastic interactions (Equation 2). The energy exponent θ controls the growth of the elastic energy fluctuations (Equation 5), the roughness exponent ζ_{eq} governs the width and wandering of equilibrium configurations, ν_{dep} rules the typical longitudinal size of thermal nuclei, and τ_{eq} is their area distribution in the presence of a small driving force f in the so-called creep regime. For $\alpha = 2$, the results are exact in $d = 1$ (53); for $d = 2$, we display the numerical results from Reference 54. For $\alpha = 1$, the results are known from functional renormalization group calculations (39). Note that θ and ζ_{eq} obey the scaling relation $\theta = 2\zeta_{eq} + d - \alpha$. For random field disorder, in $d = 1$ one expects $\zeta_{eq} = 1/3$ for $\alpha = 1$ and $\zeta_{eq} = 1$ for $\alpha = 2$.

the relation $E_{eq} \propto L^{2\zeta_{eq}} L^{-(\alpha+d)} L^{2d} \sim L^{2\zeta_{eq}+d-\alpha}$. Note that for $\alpha \geq d/2$, the interface is flat ($\zeta_{eq} = 0$), and the energy exponent saturates to the central limit value $\theta = d/2$.

At $f \to \infty$, the quenched pinning reduces to an annealed stochastic noise because in the comoving frame one has $F_p(x, u) = F_p(x, \delta u + vt) \sim F_p(x, vt)$. For short-range correlated pinning force, the strength of the disorder plays the role of an effective temperature T_{eff}. The motion is not intermittent in this so-called fast-flow regime, and one recovers the standard Edwards–Wilkinson dynamics with the generalized fractional Laplacian of Equation 2 (55). In particular, the dynamical exponent is $z = \alpha$ and the roughness exponent is $\zeta_{flow} = (\alpha - d)/2$ for $d \leq \alpha$. For a larger dimension, the Edwards–Wilkinson interface is flat.

For intermediate forces, the physics is not fully governed by any of the three characteristic points described above ($f = f_c$, $f = 0$, and $f \to \infty$). Therefore, one could wonder if a completely new scaling description should be introduced. It turns out that that it is not the case, at least for $f > f_c$. The physics of the interface can be described by a crossover between short length scales, governed by the critical behavior at $f = f_c$, and large length scales, governed by the fixed point of $f = \infty$. Below the depinning threshold, $f < f_c$, no steady state can be defined at zero temperature. The presence of a finite temperature, discussed in the next section, allows investigation of a nontrivial stationary dynamical regime (the creep) with finite velocity at forces in between the equilibrium and the depinning fixed point, and analysis of how these two fixed points affect the dynamics at different scales.

The qEW equation and its generalization to long-range elasticity are well studied and understood. In all these models, the nonstochastic part of the equation is linear in the displacement u, and one can derive the scaling relation of **Table 1**. However, in the presence of anisotropies in the disorder (56) or in the elastic interaction (57), a nonlinearity becomes relevant for short-range elasticity. In this case, the equation of motion of the interface is written as

$$\gamma \partial_t u(x,t) = c\nabla^2 u(x,t) + \lambda[\nabla u(x,t)]^2 + f + F_p(x,u). \qquad 6.$$

The inclusion of this nonlinear term affects the physical behavior as $f \to \infty$, leading to the standard Kardar–Parisi–Zhang (KPZ) (53) dynamics rather than that of the Edwards–Wilkinson. At depinning, if $\lambda f \geq 0$, the motion remains intermittent with large avalanches but with different exponents (58, 59) characterized by new scaling relations, as shown in **Table 3**. When $\lambda f < 0$, the interface develops a sawtooth shape with an effective exponent $\zeta_{dep} = 1$ (60). This regime has been recently observed in Reference 61.

Table 3 Exponents of the quenched Kardar–Parisi–Zhang (qKPZ) depinning universality class[a]

qKPZ exponent	$d = 1 \quad \alpha = 2$	$d = 2 \quad \alpha = 2$
z	1	1.1
$\zeta_{\rm dep}$	0.63	0.45
$\nu_{\rm dep}$	1.733	1.05
$\tau_{\rm dep}$	$\tau_{\rm dep} = 2 - (\zeta_{\rm dep} + 1/\nu_{\rm dep})/(d + \zeta_{\rm dep})$	
β	$\beta = \nu_{\rm dep}(z - \zeta_{\rm dep})$	

[a]The numerical values of the roughness exponent $\zeta_{\rm dep}$ are taken from Reference 50. For $d = 1$, the exponents z and $\nu_{\rm dep}$ are taken from Reference 56; for $d = 2$ these exponents are taken from Reference 58. The existence of an upper critical dimension is under debate.

3. VELOCITY AT FINITE TEMPERATURE

At finite temperature, the interface has a finite steady velocity v, even below f_c. The energy of the interface can be written as the sum of three contributions,

$$E[u] = \int_0^L \mathrm{d}^d x \left\{ \frac{c}{2} [\nabla u(x)]^2 + V_{\rm p}[x, u(x)] - f u(x) \right\}. \quad 7.$$

The first term on the right-hand side is the elastic energy of the interface; the second, the pinning potential; and the third, the energy associated to the driving force f. We note that the equation of motion (Equation 1) is obtained from $\gamma\, \partial_t u(x,t) = -\delta E[u]/\delta u(x,t)$. At finite temperature, one can write the associated Langevin equation,

$$\gamma\, \partial_t u(x,t) = c\nabla^2 u(x,t) + f + F_{\rm p}(x,u) + \eta(x,t), \quad 8.$$

with $\langle \eta(x,t)\eta(x',t')\rangle = 2\gamma T \delta(t-t')\delta(x-x')$, where the average is over different realizations of the thermal noise while the disordered landscape remains fixed.

In the presence of a finite drive, the energy (Equation 7) has no lower bound as it is tilted by the force and on average decreases linearly by increasing u. Yet, the presence of pinning generates metastable states and barriers up to f_c. The activated motion at finite temperature allows for overcoming these barriers, yielding a finite steady-state velocity.

The velocity force characteristics are represented in **Figure 3*a***. At very small force and finite temperature, a creep regime is observed, where the velocity displays a stretched exponential behavior:

$$v(f,T) = v_0 e^{-\left(\frac{f_\Gamma}{f}\right)^\mu}, \quad 9.$$

with v_0 and f_Γ dependent on the temperature and the microscopic parameters, whereas μ is a universal exponent. This creep law was verified experimentally first by Lemerle et al. in ferromagnetic ultrathin films with $\mu \simeq 1/4$ (62; see **Figure 3*b***). Rather strikingly, this law can span several decades of velocity (from almost walking speed to nail-growth speed) by just varying one decade of the externally applied magnetic field at ambient temperature. The creep law was subsequently found by many other experiments (63, 64; see Section 6 for a brief review), confirming the universality and robustness of several creep properties. Such universality naturally calls for minimal statistical-physics models, on which we focus below.

Equation 9 has been predicted in References 65–67 and derived within the FRG technique in Reference 46. The stretched exponential behavior originates from the collective nature of the low-temperature dynamics of these extended objects. For a point-like system embedded in a short-range disorder potential, the response to a small force is linear in f. The idea is to consider that the energy landscape is characterized by valleys at a distance Δu separated by an energetic barrier

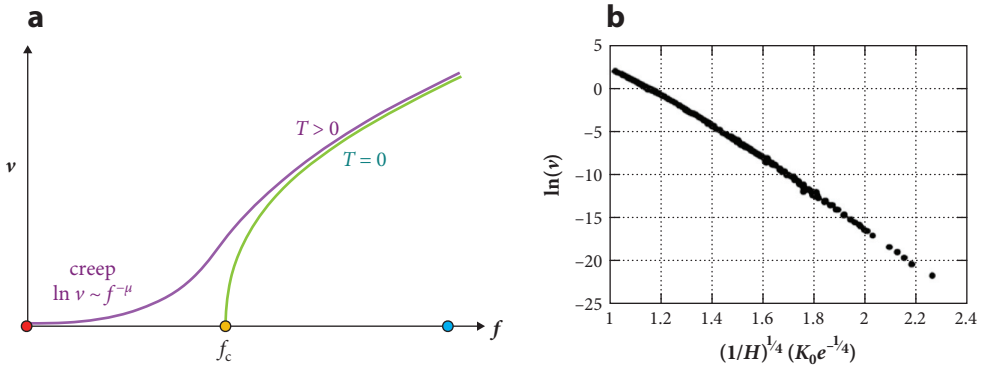

Figure 3

(*a*) Velocity force characteristics at finite temperature. When f is very small compared to f_c and at very small temperature, one observes the creep law $\ln v \sim f^{-\mu}$. Panel *a* adapted from Reference 25. (*b*) First experimental verification of a creep law consistent with $\mu = 1/4$ in 2D ultrathin Pt/Co/Pt film at room temperature. Panel *b* adapted from Reference 62.

of typical size E_p. In the presence of the tilt introduced by a finite force f, the energy gap between two consecutive valleys becomes $\sim f\Delta u$ (see **Figure 4**). According to the Arrhenius law, the time to jump from left to right will be $e^{\beta(E_p - f\Delta u/2)}$, whereas the time for jumping from right to left would be $e^{\beta(E_p + f\Delta u/2)}$. Therefore, the velocity can be computed as the thermally assisted flux flow (TAFF; 68, 69) across the barrier:

$$v \propto e^{-\beta(E_p - f\Delta u/2)} - e^{-\beta(E_p + f\Delta u/2)} \simeq e^{-\beta E_p}\Delta u f. \qquad 10.$$

We conclude that, in the presence of bounded barriers, the velocity will be linear even with exponentially suppressed mobility.

For an extended object, the typical barrier grows when the external force vanishes and its divergence is at the origin of the stretched exponential behavior in Equation 9. In **Figure 5**, we show different configurations obtained at different times from the direct integration of Equation 8. At

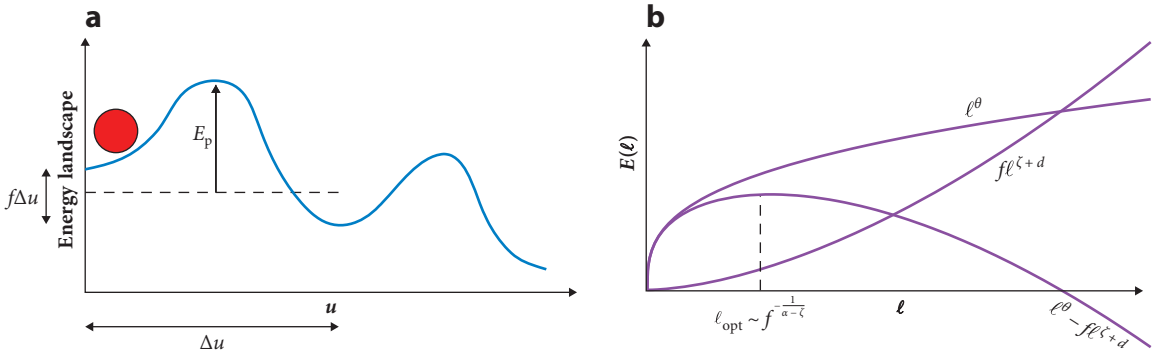

Figure 4

(*a*) Thermally assisted flux flow. The activated velocity of a single degree of freedom in a short-range disordered potential is linear in the force and exponentially suppressed by the size of the typical barrier, E_p. (*b*) Creep behavior. The energetic barrier encountered by an interface diverges when the applied force vanishes. Indeed, in order to find a new metastable state characterized by smaller energy, a large portion of the interface has to reorganize. Scaling arguments predict that the linear size of such reorganization scales as $\ell_{opt} \sim f^{-\frac{1}{\alpha - \zeta_{eq}}}$.

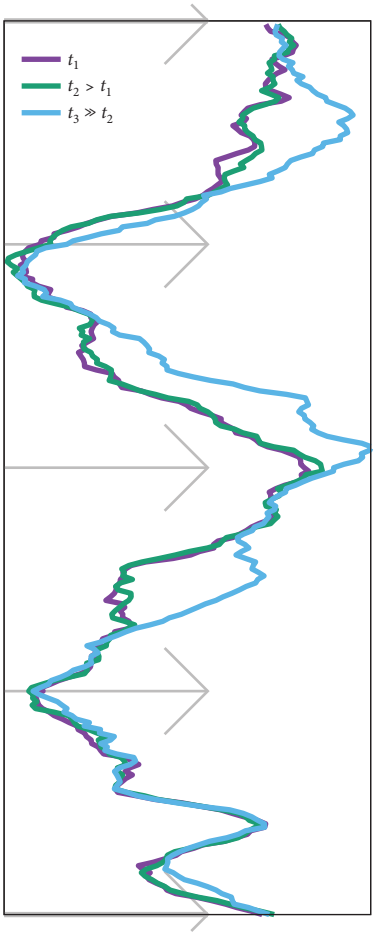

Figure 5

Configurations at different times obtained by direct integration of Equation 8. Incoherent oscillations are observed at short times, and the configurations differ only at short length scales. At much longer times, the line advances in the direction of the force with a coherent excitation that involves a large reorganization.

short times, one observes incoherent oscillations and the configurations differ only at short length scales. At much longer times, the line advances in the direction of the force with a coherent excitation that involves a large reorganization. This collective motion leads the system to a local minimum characterized by a lower energy due to the presence of the force. It is very unlikely that the interface will climb back to the previous configurations characterized by a higher energy. This new and deeper valley is the starting point of a new search in the forward direction. At these timescales, the dynamics of the line can be seen as a sequence of metastable states,

$$\alpha_1 \rightarrow \alpha_2 \rightarrow \alpha_3 \rightarrow \ldots, \qquad 11.$$

characterized by decreasing energies

$$E_{\alpha_1} > E_{\alpha_2} > E_{\alpha_3} > \ldots. \qquad 12.$$

At low temperature and starting from a given metastable state α_1, among all metastable states with lower energy, the one that we reach by crossing the minimal barrier is α_2. From α_2, a new minimal

barrier crossing takes us to α_3, and so on. It is possible to show that for an interface of internal dimension d embedded in a $d+1$ dimension, the pathway obtained with such a rule is the optimal one (and thus the one that dominates the statistics of the dynamics) in the low-temperature limit (70).

The first attempts to evaluate the barriers and the length scales associated to this coarse-grained dynamics have been conducted in References 65 and 66 and in Reference 46 via FRG. The main assumption in their original derivations is that, during the dynamical evolution, the energy barriers scale as the energy fluctuations of the ground state at $f = 0$. At equilibrium, the fluctuations of the free energy are known to grow with the system size with a characteristic exponent θ that depends on the equilibrium roughness exponent via an exact scaling relation $\theta = 2\zeta_{\rm eq} + d - \alpha$. Numerical simulations in Reference 71 have shown that the barriers separating two equilibrium metastable states, which differ on a portion ℓ, grow as ℓ^{ψ} with an exponent consistent with $\psi \simeq \theta$. Using these ideas, one can assume that the energy barriers due to the pinning centers and in absence of tilt grow with the size of the reorganization,

$$E_{\rm p}(\ell) \sim \ell^{\theta} = \ell^{2\zeta_{\rm eq}+d-\alpha}. \qquad 13.$$

If the motion is in the forward direction, one must subtract the energy induced by the tilt,

$$E_{\rm f}(\ell) \sim f\, u(\ell)\, \ell^{d} = f\ell^{\zeta_{\rm eq}+d}. \qquad 14.$$

In **Figure 4*b***, we show that the competition between these two terms (Equations 13 and 14) yields the characteristic length scale $\ell_{\rm opt}$ of the optimal reorganization [and the optimal barrier $E_{\rm p}(\ell_{\rm opt})$], allowing a new metastable state with a lower energy to be reached:

$$\ell_{\rm opt} \sim f^{-\frac{1}{\alpha-\zeta_{\rm eq}}}, \qquad E_{\rm p}(\ell_{\rm opt}) \sim f^{-\frac{\theta}{\alpha-\zeta_{\rm eq}}}. \qquad 15.$$

Using the scaling of $E_{\rm p}$ in Equation 10, one recovers the creep law, Equation 9, and identifies the creep exponent,

$$\mu = \frac{\theta}{\alpha-\zeta_{\rm eq}} = \frac{2\zeta_{\rm eq}+d-\alpha}{\alpha-\zeta_{\rm eq}}, \qquad 16.$$

as an equilibrium exponent. Particularly in $d = 1$, for RB disorder and short-range elasticity, one recovers $\mu = 1/4$ as in the experiment (62).

Although for the average velocity there is excellent agreement between the simple scaling arguments (65, 66, 69) and the more sophisticated FRG analysis (46), the FRG showed clearly that other length scales besides $\ell_{\rm opt}$ (see **Figure 4*b***) were necessary to describe the motion, which points to rich dynamics in the creep regime. In particular, the FRG showed that in the dynamics the thermal nucleus led to avalanches at larger length scales than $\ell_{\rm opt}$ itself. To make a full analysis of the creep regime, a numerical investigation was thus eminently suitable. However, this is a highly nontrivial task considering the exponentially large timescales and length scales. We discuss how to undertake such a study in the next section.

4. NUMERICAL METHODS

The direct simulation of the Langevin Equation 8 has been performed in Reference 67 and later in Reference 72. This approach confirms a nonlinear behavior for the velocity-force characteristics but fails in probing the specific scaling of the creep law. In fact, at low temperature, these methods can focus only on the microscopic dynamics describing incoherent and futile oscillations around local minima (see **Figure 5**). The forward motion that allows escape from these minima occurs at

very long timescales that are difficult to reach. In practice, one must increase the temperature or the force bringing the system beyond the validity of the creep scaling hypothesis.

A completely different strategy focuses on the coarse-grained dynamics at the timescales of the coherent reorganizations that are able to lower the energy. In practice, one must model the interface as a directed polymer of L monomers at integer positions $u(i)$, where $i = 1, \ldots, L$, and with periodic boundary conditions $[u(L + 1) = u(1)]$. The energy of the polymer is given by

$$E = \sum_i \left\{ [u(i+1) - u(i)]^2 - f u(i) + V[i, u(i)] \right\}. \quad 17.$$

To reduce the configuration space, it is useful to implement a hard metric constraint such that

$$|u(i+1) - u(i)| \leq \kappa, \quad 18.$$

with $\kappa \sim \mathcal{O}(1)$ being an integer.

To model RB disorder, one can define $V_{\mathrm{RB}}(i, u) = R_{i,u}$ with $R_{i,u}$ being Gaussian random numbers with zero mean and unit variance, whereas for RF disorder $V_{\mathrm{RF}}(i, u) = \sum_{k=0}^{u} R_{i,k}$, such that $\overline{[V_{\mathrm{RF}}(i, j) - V_{\mathrm{RF}}(i', j')]^2} = \delta_{i,i'} |j - j'|$.

At the coarse-grained level, the dynamics corresponds to a sequence of polymer positions determined using a two-step algorithm.

- **Thermal activation:** Starting from any metastable state, one must find the compact rearrangement that decreases the energy by crossing the minimal barrier among all possible pathways.
- **Deterministic relaxation:** After the above activated move, the polymer is not necessarily in a new metastable state and relaxes deterministically with the nonlocal Monte Carlo elementary moves introduced in Reference 73.

From the computational point of view, the most difficult task is in the first step. In principle, one fixes a maximal barrier and enumerates all possible pathways that stay below the maximal allowed energy. If one of them reaches a state with a lower energy, the thermal activation step is over; otherwise the maximal barrier is increased and the process is repeated. This protocol is exact; it has been implemented in Reference 70, but it has severe computation limitations at low forces as the minimal barrier is expected to diverge for vanishing forces. In order to explore the low-force regime, a different strategy has been adopted in Reference 74. Instead of looking to the pathway with the minimal barrier, one selects the smallest rearrangement that decreases the energy. This is done by fixing a window w and computing the optimal path between two generic points i and $i + w$ of the polymer using Dijkstra's algorithm adapted to find the minimal energy polymer between two fixed points. The minimal favorable rearrangement corresponds to the minimal window for which the best path differs from the polymer configuration. Using this strategy, it was possible not only to increase the system size by a factor of 30 but also, and more importantly, to decrease the external drive f by a factor of 100, unveiling the genuine creep dynamics.

5. CREEP DYNAMICS IN THE LIMIT OF VANISHING TEMPERATURE

Here, we give a summary of the main results obtained using the coarse-grained dynamics introduced in References 70 and 74. The output of the algorithm is a sequence of metastable states α_k ($k = 1, \ldots, n$), as shown in **Figure 6**. In Reference 70, E_{p} is the minimal barrier among all possible pathways, whereas in Reference 74 the criterion of the minimal barrier has been approximated with the criterion of the minimal rearrangement, which allows for reaching much smaller

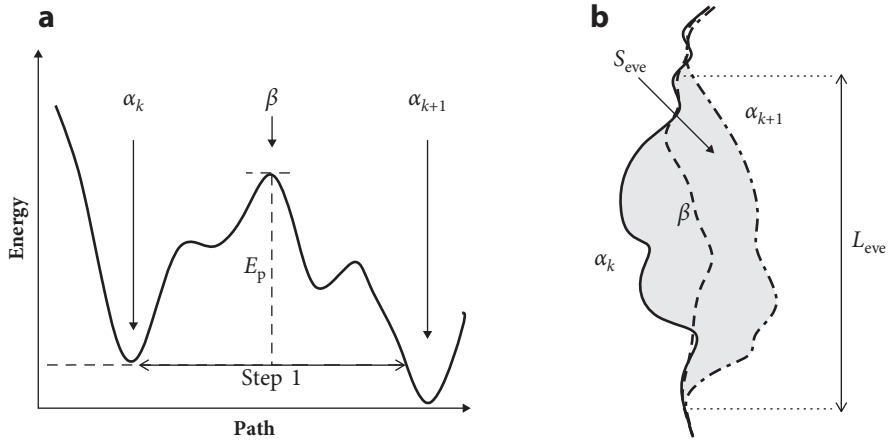

Figure 6

Sketch of the selected pathway starting from the metastable state, α_k. (*a*) During step one of the algorithm, one searches for a polymer configuration with an energy smaller than the one associated to α_k by crossing a minimal barrier E_p. (*b*) The polymer relaxes deterministically to a metastable configuration; no barriers are overcome at this stage. Figure adapted from Reference 70.

forces and much larger sizes. The area between two subsequent metastable states (see **Figure 6**) defines the size of an activated event. Below this size, the dynamics is futile, being characterized by incoherent vibrations, whereas once the new metastable state is reached the backward move is suppressed.

5.1. Statistics of the Events and Clusters

From the scaling arguments of Section 3, one expects that the area of the activated events is of the order $\ell_{opt}^{d+\zeta_{eq}}$ with ℓ_{opt}, which grows when the force decreases (see Equation 15). However, the distribution shown in **Figure 7** displays a power-law scaling analogous to the depinning one,

$$P(S_{eve}) \sim S_{eve}^{-\tau} g(S_{eve}/S_c). \quad 19.$$

When the force decreases, the cutoff $S_c(f)$ grows and displays the scaling predicted in Section 3:

$$S_c \sim \ell_{opt}^{d+\zeta_{eq}} \sim f^{-\nu_{eq}(d+\zeta_{eq})}. \quad 20.$$

Here, $d = 1$ and ζ_{eq} depends on the nature of the disorder: For RB, $S_c(f) \sim f^{-5/4}$, whereas for RF, $S_c(f) \sim f^{-2}$.

Equation 19 implies that the typical activated events are much smaller than the one predicted by scaling arguments. However, few very large events dominate the characteristic timescales of the forward motion. The behavior of the velocity in the creep formula is then determined by the occurrence of such large reorganizations. Indeed, the barriers associated with the largest elementary events are expected to scale as

$$U_{opt}(f) \sim \ell_{opt}^{\theta} \approx S_c(f)^{\theta/(d+\zeta_{eq})}. \quad 21.$$

Then the mean velocity in the Arrhenius limit is written as

$$v \sim \exp[-U_{opt}/T] \sim \exp[-(f_T/f)^{\mu}/T], \quad 22.$$

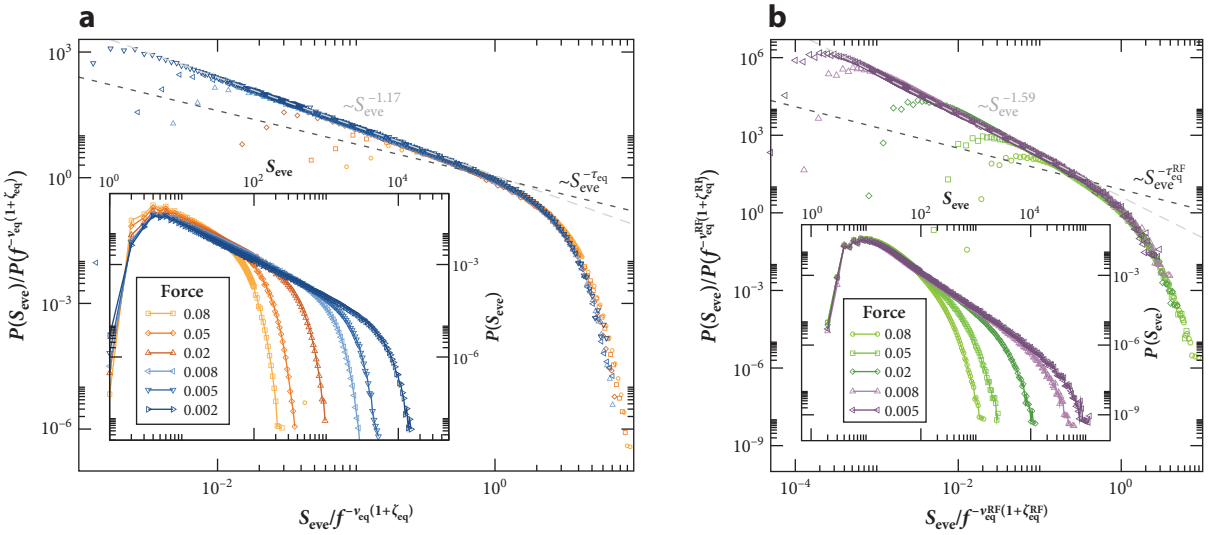

Figure 7

Events size distributions $P(S_{eve})$ for RB (*a*) and RF (*b*) at different forces. Main panels show collapses by plotting S_{eve}/S_c with $S_c(f) = f^{-\nu_{eq}(1+\zeta_{eq})}$. Insets show the unscaled distributions. Note that for RB disorder, $S_c(f) = f^{-5/4}$, whereas for RF disorder, $S_c(f) = f^{-2}$. The perfect collapse validates the expected creep scaling, $\ell_{opt} \sim f^{-\nu_{eq}}$, given $S_c \sim \ell_{opt}^{(1+\zeta_{eq})}$. Figure adapted from Reference 74. Abbreviations: RB, random bond; RF, random field.

with $\mu = \theta/(2 - \zeta_{eq})$, recovering the correct formula for the mean velocity, i.e., the celebrated creep law of Equation 9. The main difference with the previous scaling approaches (65, 66) is that the creep law is determined not by the typical events but by the largest ones instead.

To get further insight on the sequence of these events, one notes that the exponent τ of $P(S_{eve})$ is larger than the one expected in equilibrium (in particular in **Figure 7**, for RB, $\tau = 1.17$ instead of $\tau_{eq} = 4/5$ and, for RF, $\tau = 1.59$ instead of $\tau_{eq} = 1$). The anomaly observed in the exponent τ is the first fingerprint of a discrepancy between creep events distributions and other types of avalanches, such as the depinning ones, going well beyond the anticipated differences of critical exponents. In **Figure 8**, the typical sequence of avalanches is randomly located in space, whereas the creep events are organized in spatiotemporal patterns very similar to those of earthquakes: The large events are the main shocks that are followed by a cascade of small activated events. The events in the cascade are analogous to the aftershocks that are responsible for an excess of small events in the Gutenberg–Richter exponent as reported also in the analysis of real earthquakes (31, 33, 75).[3] Similar patterns for the elementary activated events were observed below but near the depinning threshold (76).

In order to analyze the spatiotemporal patterns, one can study the clusters of correlated events, defined by the activated events enclosed by a circle in **Figure 8**. All details in the definition of the clusters are found in Reference 74.

Surprisingly, for both RB and RF disorders, the statistics of the clusters appear as one of the depinning avalanches with $\tau_{dep} = 1.11$ and the cutoff controlled by the system size and diverging in the thermodynamic limit (27; see **Figure 9**).

[3]The Gutenberg–Richter exponent, $b = \frac{3}{2}(\tau - 1)$, for the earthquake magnitude distribution should be smaller than the mean-field prediction of 3/4, but from seismic records one gets (31, 33) $b \simeq 1$.

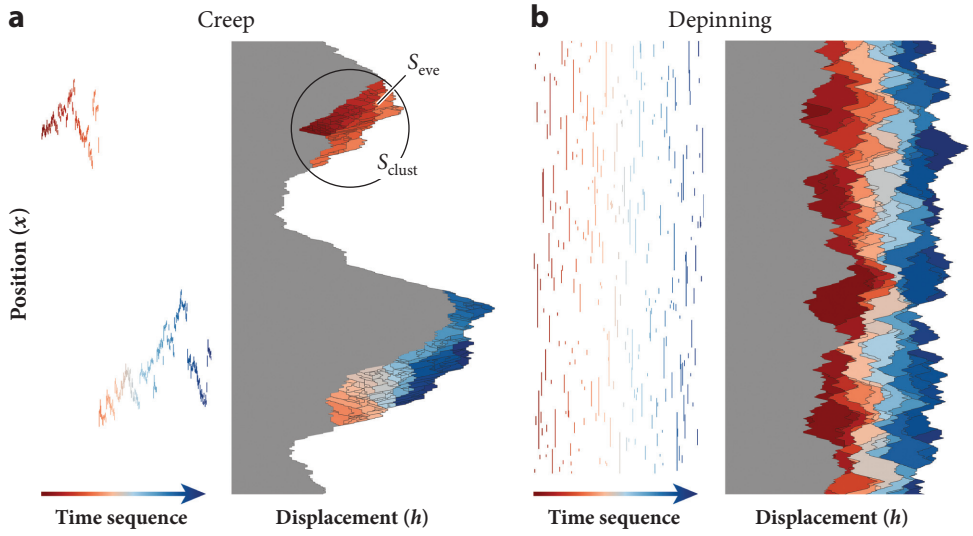

Figure 8

(*a*) Sequence of activated events in the creep regime. First, in the activity map, each segment corresponds to an event and displays its longitudinal length. The full configurations of 300 consecutive metastable states are shown immediately after. An individual event of size S_{eve} and a cluster of size S_{clust} are exemplified. (*b*) Sequence of deterministic avalanches close to the depinning that appear randomly distributed in space. Again, both activity map and sequence of configurations are shown. Figure adapted from Reference 74.

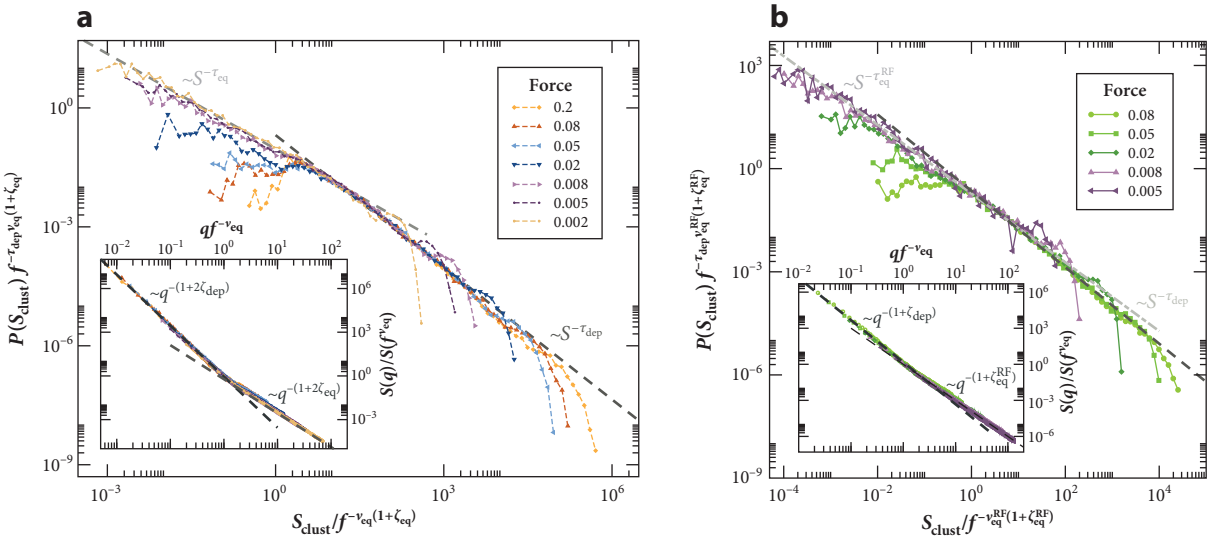

Figure 9

Cluster area distribution $P(S_{clust})$ for different forces for random bond (*a*) and random field (*b*) disorder. A characteristic size $S_c(f)$ separates small clusters that follow equilibrium-like statistics from big clusters that follow a depinning-like one. This result is confirmed by the study of the rescaled structure factor $S(q)$ for the same forces (*insets*): a geometrical crossover is observed from equilibrium-like roughness at small scales to a depinning-like roughness at large scales. Figure adapted from Reference 74.

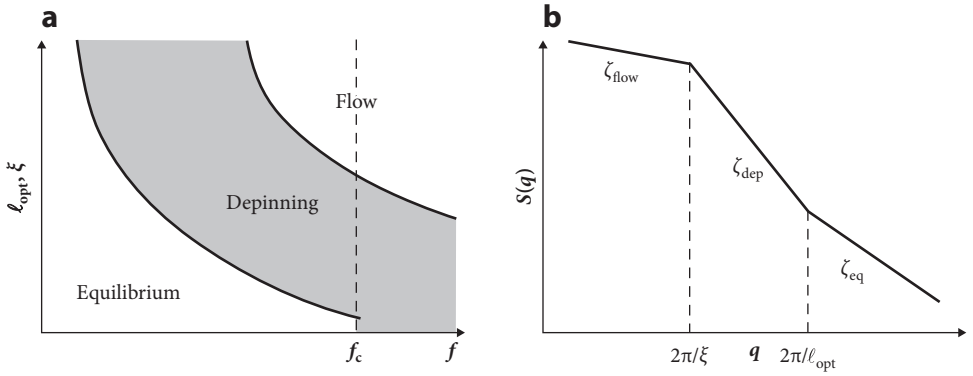

Figure 10

(*a*) Dynamical phase diagram proposed in Reference 46 at finite temperature. Below f_c, the crossover between equilibrium and depinning occurs at the scale ℓ_{opt}. At finite temperature, there is also a crossover at a length scale ξ between depinning and fast flow. However, ξ diverges in the limit of small temperature. (*b*) Behavior of the roughness measured from the structure factor consistent with the dynamical phase diagram. Figure adapted from Reference 70.

5.2. Geometry of the Interface

An independent and complementary confirmation of these results comes from the study of the roughness of the interface at different scales as introduced in Reference 70. In practice, one measures the structure factor,

$$S(q) = \overline{u(q)u(-q)} \sim q^{-(d+2\zeta)}, \qquad 23.$$

where $u(q)$ is the Fourier transform of the position of the interface and the overline represents the average over many configurations. The insets of **Figure 9** show that there exists a crossover $1/q_c \sim \ell_{opt}$ between two different behaviors of the roughness: At small length scales the interface seems to be at equilibrium, whereas at large length scales it appears at depinning. This observation supports the idea that the clusters are depinning-like above a scale ℓ_{opt}. Although such a result is consistent with the predictions obtained by FRG in Reference 46, it should be stressed that these clusters with depinning statistics above ℓ_{opt} are formed by several activated events rather than generated by a single deterministic move.

The coarse-grained dynamics studied here is in the limit of vanishing temperature. At finite temperature, the velocity is nonzero; this induces the fast flow roughness to become relevant at large length scales (see **Figure 10**). The crossover occurs at a scale ξ that diverges at vanishing temperature. The FRG proposes a scaling form for ξ at low temperature and force that depends on f and T (46), but this form was never tested in numerical simulation or experiments.

The roughness exponent measured at large scales $\zeta_{dep} \approx 1.25$ (see the *inset* of **Figure 9**) is in agreement with the depinning exponent of the qEW universality class. The qEW depinning exponents are expected when the elastic interactions are harmonic and short range as in Equation 7. When the interactions are anharmonic (57, 77) or a metric constraint such as that in Equation 18 is present, the depinning is in the quenched KPZ (qKPZ) universality class. In particular, the roughness exponent is expected to be $\zeta_{dep}^{qKPZ} \approx 0.63$ (57, 70). The reasons why simulations deep in the creep regime (but with the metric constraint of Equation 18) display a crossover from ζ_{eq} to ζ_{dep} instead of a crossover from ζ_{eq} to ζ_{dep}^{qKPZ} are analyzed by E.E. Ferrero, L. Foini, T. Giamarchi, A.B. Kolton, and A. Rosso (manuscript in preparation). The exponents of the qEW universality class show up at an intermediate regime, but at very large scales the qKPZ exponents

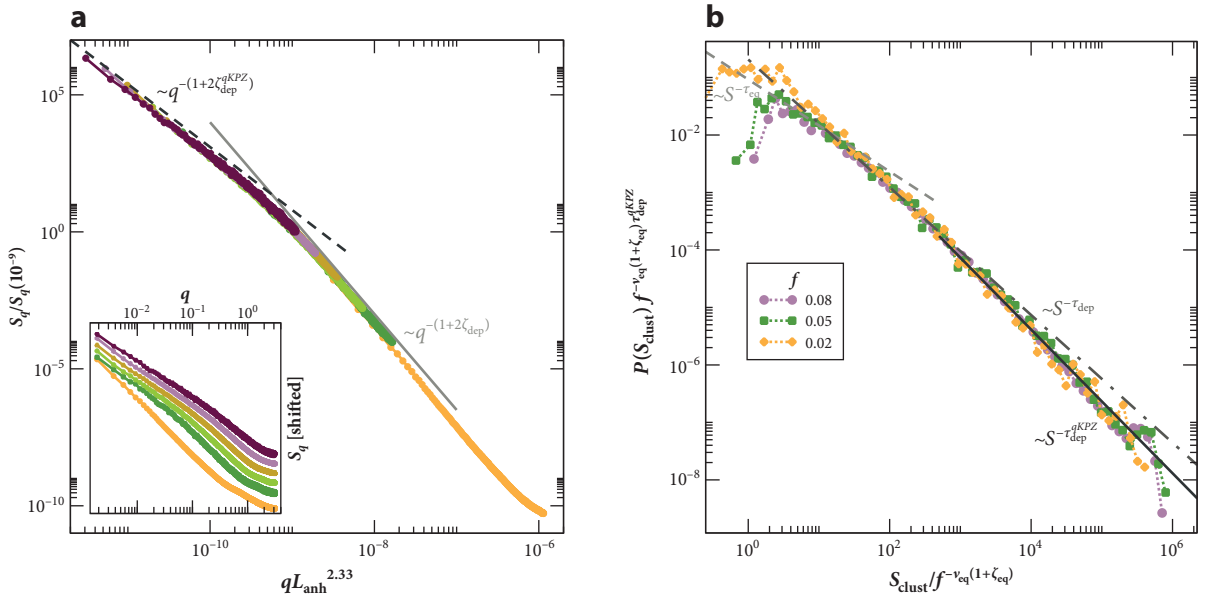

Figure 11

(*a*) Structure factor for the RB case showing the characteristic length scale, L_{anh}, which separates the harmonic depinning regime with roughness exponent ζ_{dep} from the anharmonic depinning regime with exponent ζ_{dep}^{qKPZ}, for different high forces $f \in \{0.2, 0.5, 0.6, 0.7, 0.8, 0.9\}$, $L = 3{,}360$. The bottom-left inset shows the raw structure factor arbitrarily shifted in the vertical direction for different forces for a better display. The main panel shows the structure factor rescaled with $L_{anh} \propto (\ell_{opt}/L_c)^{7/3}$, as proposed in Equation 24 for RB disorder. Straight gray lines are a guide to the eye, showing slopes corresponding to $\zeta_{dep} \simeq 1.25$ (*solid gray line*) and $\zeta_{dep}^{qKPZ} \simeq 0.65$ (*dashed gray line*). (*b*) Cluster-size distributions for $L = 3{,}360$ and $f \in \{0.2, 0.5, 0.8\}$. The anharmonic crossover has consequences in the cluster distribution for large cluster sizes. In the depinning regime, the power-law decay has a crossover from a regime described by $\tau_{dep} \approx 1.11$ to a regime described by $\tau_{dep}^{qKPZ} \approx 1.25$ indicated by the two dashed lines. Abbreviation: RB, random bond.

are recovered, as expected. The crossover between the two depinning regimes is estimated to be

$$L_{anh} \propto \ell_{opt}^{\frac{\zeta_{dep}-\zeta_{eq}}{\zeta_{dep}-1}}. \qquad 24.$$

The crossover occurs at very large sizes for small forces, and it cannot be observed numerically. However, at larger forces the crossover can be observed as shown in **Figure 11*a*** for the structure factor and in **Figure 11*b*** for the cluster size statistics.

5.3. Optimal Paths and Barriers

The exact algorithm for simulating the coarse-grained dynamics below the depinning threshold is computationally expensive but has the advantage of giving access to the energy barriers of the activated motion (70). If the interface moves on a torus (namely, periodic boundary conditions are assumed in both x and u), the dynamics reaches a stationary state independent of the initial condition, with a finite sequence of metastable states α_k separated by barriers $E_p(\alpha_k \to \alpha_{k+1})$ that can be computed exactly.

Barriers are important, because the Arrhenius activation formula tells us that at vanishing temperatures the steady-state forward motion of the elastic interface is fully controlled in a finite

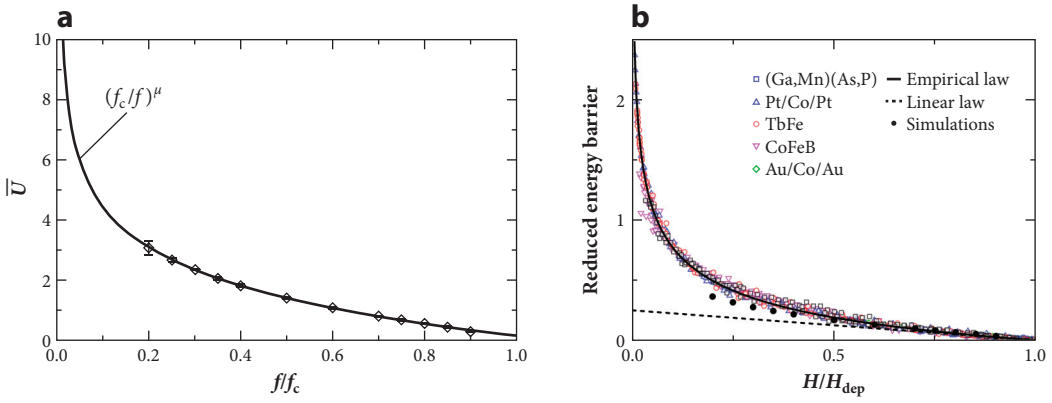

Figure 12

(*a*) Average over disorder realizations of the dominant barrier, as obtained by using the exact transition pathways algorithm. Panel adapted from Reference 70. (*b*) Rescaled energy barrier as a function of H/H_{dep} for different materials and temperatures ranging from 10 to 315 K (25 curves in total). Black circles correspond to the barriers shown in panel *a*. Panel adapted from Reference 78.

sample by the largest barrier $U = \max_k E_p(\alpha_k \to \alpha_{k+1})$ encountered in the stationary sequence of metastable states. The dominant configuration α_{k^*} such that $U = E_p(\alpha_{k^*} \to \alpha_{k^*+1})$ is the largest barrier in a given sample plays a role similar to a ground-state configuration in an equilibrium system, in the sense that its attributes tend to dominate the average properties at low enough temperatures (compared with the gap between the first- and second-largest energy barriers).

In **Figure 12*a***, we show the mean value $\overline{U}$ as a function of the force. As expected from the creep formula, $\overline{U}$ grows with decreasing force. Unfortunately, the computational cost of applying the exact algorithm is too high to verify the asymptotic scaling $\overline{U} \sim f^{-\mu}$ when $f \to 0$. When $f \to f_c$, the barrier vanishes and the size of the activated event becomes of the order of the Larkin length, the length for which the relative displacements are of the order of the interface thickness (or the correlation length of the disorder; 24). This matches nicely with the behavior expected for the critical configuration at $f = f_c$. There, the barrier is zero as the configuration is marginally stable and the soft mode is localized (Anderson-like) with a localization length that can be identified with the Larkin length (79). In **Figure 12*b***, we show the same quantity obtained in experiments for different ferromagnetic domain walls.

6. COMPARISON WITH EXPERIMENTS

The creep regime has been studied in different types of domain walls. Paradigmatic examples are domain walls in thin film ferromagnets with out-of-plane anisotropy (12), driven by an external magnetic field or by an external electric current. In these systems, the domain walls can be directly observed by microscopy techniques based on the magneto-optic Kerr effect (MOKE). This makes measuring the mean velocity as a function of the applied field and the domain wall geometry possible. More recently, the analysis of the images has allowed identification of the sequence of events connecting different metastable domain wall configurations in the presence of a uniform weak drive. In this section, we briefly review part of such experimental literature. For a dedicated review of the experimental literature on magnetic domain walls up to 2013, including reports of different values of μ and strong pinning issues, see Reference 12. As a side remark, we also mention the possibility of studying the creep regime of domain walls in ferroelectric materials driven by an external electric field and observed with piezoelectric force microscopy (14, 15).

6.1. Creep Velocity

The creep law (Equation 9) was first experimentally tested in thin ferromagnetic films (Pt/Co(0.5 nm)/Pt) driven by a magnetic field H by Lemerle et al. (62). They observed a clear stretched exponential behavior ($\log v \propto -H^{-\mu}$) of the stationary mean velocity as a function of the applied field. Rather strikingly, such law can span several decades of velocity, from almost walking speeds to the speed of nail growth. The creep exponent μ was found to be compatible with the prediction $\mu = (2\zeta_{eq} - 1)/(2 - \zeta_{eq}) = 1/4$, where the equilibrium roughness $\zeta_{eq} = 2/3$ corresponds to an RB disorder. A confirmation of the validity of the creep predictions was reported later in a study of Ta/Pt/$Co_{90}Fe_{10}$(0.3 nm)/Pt ferromagnetic thin film wires (63). In this paper, not only Equation 9 with $\mu \approx 1/4$ was verified but also a dimensional crossover (d: $1 \to 0$) was observed in the velocity force characteristic at low field. Indeed, by decreasing the magnetic field, the length scale ℓ_{opt} grows as $\sim H^{-\nu_{eq}}$ with $\nu_{eq} = 1/(2 - \zeta_{eq})$ up to the size of the wire's width at which point it saturates. Consequently, the barrier $E_p \sim \ell_{opt}^{\theta}$ saturates, inducing the breakdown of the creep law of Equation 9 when ℓ_{opt} becomes of the order of the wire width. A dimensional crossover (d: $1 \to 0$) then takes place, from creep, Equation 9, to a TAFF-like regime, Equation 10.

From the creep theory perspective, the experiments of References 62 and 63 hence provide crucial information: (*a*) Although domain walls are actually two-dimensional objects in three-dimensional materials, they effectively behave as a simpler one-dimensional elastic object. In other words, the thickness of the magnetic film is smaller than ℓ_{opt} and the dynamics is governed by energy barriers with $\theta(d = 1)$. (*b*) Dipolar interactions originated by stray magnetic fields seem to be unimportant, otherwise the nonlocal elasticity would change the exponent μ. (*c*) The disorder is of RB type, as for RF disorder one expects $\zeta_{eq} = 1$, yielding $\mu = 1$. This is particularly relevant, because the nature of the domain wall pinning is one of the less controlled properties of the hosting materials.

Because of the pioneering work by Lemerle et al. (62), there have been several recent works in thin magnetic systems reporting a consistent creep behavior with a mean domain wall velocity showing a stretched exponential law with $\mu = 1/4$ at low-enough driving fields (12, 64, 78, 80–87) and for different temperatures (78). The energy barrier encountered by the wall has been estimated using the Arrhenius formula $U = -K_B T \log v/v_0$, with v_0 being a characteristic field-independent velocity (64). Its behavior as a function of H was found to be universal for a large family of materials: U diverges at small fields as predicted by the creep law, $U \sim H^{-\mu}$, and vanishes at the depinning field as $U \sim (H - H_d)$ (see **Figure 12*b***). Both asymptotic behaviors are well described by the matching expression $U \sim [1 - (H_d/H)^{\mu}]$. Furthermore, the behavior experimentally observed for U as a function of H is in perfect agreement with the value $\overline{U}$ found in Reference 70 shown in **Figure 12*a***.

6.2. The Roughness Puzzle

Another important test of the creep theory is to study the steady-state roughness of the interface. From **Figure 10**, we expect that the width of a domain wall of size L and $w(L)$ (see Equation 3) should scale as

$$w^2(L) \sim \begin{cases} L^{2\zeta_{eq}} & \text{if } L < \ell_{opt} \\ L^{2\zeta_{dep}} & \text{if } \ell_{opt} < L < \xi \\ L^{2\zeta_{flow}} & \text{if } \xi < L. \end{cases} \quad 25.$$

Lemerle et al. (62) and various following works report $\zeta \approx 0.7 \pm 0.1$, in agreement with the equilibrium value $\zeta_{eq} = 2/3$ but far from the depinning qEW universality class $\zeta_{dep} = 1.25$. As we discuss below, however, in the light of the current theory for creep and more recent experiments,

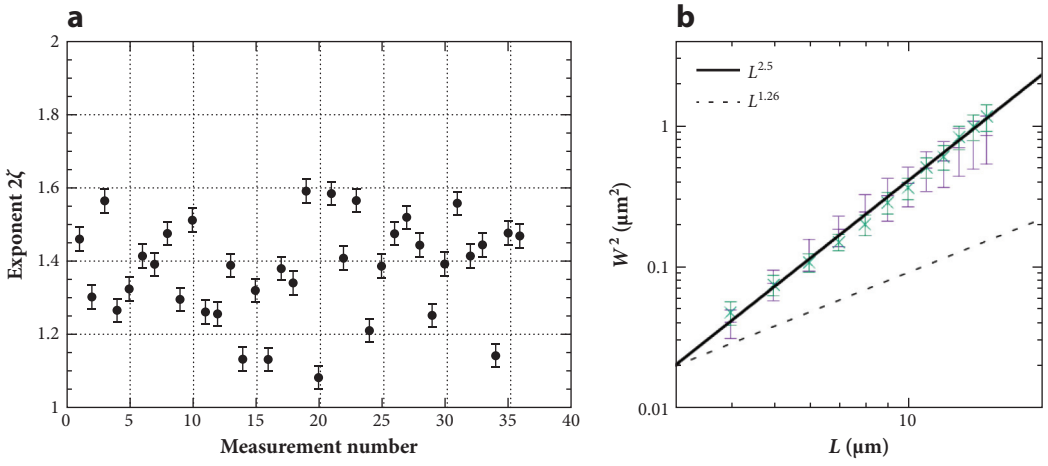

Figure 13

(*a*) Roughness exponents obtained in Reference 62 by fitting the displacement correlator function $\overline{[u(x+L)-u(x)]^2} \sim L^{2\zeta}$ with $1\,\mu\text{m} < L < 15\,\mu\text{m}$ and $v = 7$ nm/s. The average exponent is $\zeta \approx 0.69 \pm 0.07$. (*b*) Roughness exponent obtained in Reference 84 by fitting the detrended width. Different symbols correspond to two domain wall configurations at $v \approx 2$ nm/s. The solid line indicates a quenched Edwards–Wilkinson scaling $2\zeta_{\text{dep}} \approx 2.5$, and the dashed line indicates a quenched Kardar–Parisi–Zhang scaling $2\zeta_{\text{dep}}^{\text{qKPZ}} = 1.26$.

the identification of the observed ζ with $\zeta_{\text{eq}} = 2/3$ cannot be justified, calling for a new reinterpretation of the data.

Recently, Gorchon et al. (78) studied field-driven domain walls in the prototypical ultrathin Pt/Co(0.45 nm)/Pt ferromagnetic films. By fitting the velocity force characteristics in the creep and depinning regimes, they determined the critical depinning field $H_{\text{dep}} \approx 1{,}000$ Oe and a characteristic energy scale $T_{\text{dep}} \approx 2{,}000\,K$ at room temperature ($T = 300\,K$). With these values it is possible to estimate ℓ_{opt} using the assumptions of weak pinning (88–90):

$$\ell_{\text{opt}} = L_{\text{c}}(H_{\text{dep}}/H)^{\nu_{\text{eq}}},$$
$$L_{\text{c}} = (k_{\text{B}}T_{\text{dep}})/(M_{\text{s}}H_{\text{dep}}w_{\text{c}}\delta). \qquad 26.$$

The microscopic Larkin length L_{c} can be evaluated as a function of the domain wall width w_{c}, the thickness of the sample δ, and the saturation magnetization M_{s}. All these micromagnetic parameters are known, yielding $L_{\text{c}} \approx 0.04\,\mu\text{m}$ (see Reference 83 for the analysis for different materials). Using a spatial resolution of 1 μm, typical for MOKE setups and the measured $H_{\text{dep}} \approx 1{,}000$ Oe, one can get the condition $H \lesssim 0.4$ Oe at room temperature to resolve the typical thermal nucleus size, i.e., $\ell_{\text{opt}} > 1\,\mu\text{m}$. Interestingly, ℓ_{opt} was estimated in Ta/Pt/$Co_{90}Fe_{10}$(0.3nm)/Pt wires (63) with a completely different method, observing finite size effects as the wire width w was reduced. A good scaling $\ell_{\text{opt}} \sim H^{-\nu_{\text{eq}}}$ with one-dimensional RB exponents, compatible with $\zeta_{\text{eq}} = 2/3$, was found. For these samples a field of $H = 16$ Oe gives $\ell_{\text{opt}} \approx 0.16\,\mu\text{m}$, which is remarkably in good agreement with the above estimate for the Pt/Co/Pt film. Unfortunately, no direct roughness exponent measurements were reported in Reference 63 (see **Figure 13**). The above estimates suggest that the range of length scales used to fit experimentally the roughness exponent exceeds the size of ℓ_{opt}. This implies that the value $\zeta \sim 0.6$–0.7 recorded in References 62, 86, and 91–93 cannot be interpreted as an equilibrium exponent and must actually correspond to the depinning regime or to the fast flow regime of roughness (see **Figure 2**).

The fast flow exponent predicted for RB or RF systems is $\zeta_{\text{flow}} = 1/2$, which is quite far from the observed values. For short-range elasticity there are two universality classes at the depinning transition: the qEW with a roughness exponent $\zeta_{\text{dep}} \simeq 1.25$ and the qKPZ with $\zeta_{\text{dep}}^{\text{qKPZ}} \simeq 0.63$. The first value is consistent with the roughness exponent obtained in Reference 84 at low velocity, whereas the second value is remarkably close to the values at higher velocity reported in Reference 62. A possible way to solve this puzzle is to invoke a crossover qEW–qKPZ already observed in the numerical simulations in Section 5.2. There, at low drive, the crossover occurs at very large length scales, and the qEW exponents are measured. At higher drive the qKPZ is recovered already at short distances. To invoke such an identification, however, we have to justify the presence of a KPZ term in the effective domain wall equation of motion. At least two mechanisms can justify the presence of a nonlinear KPZ term: (*a*) A kinetic mechanism yields $\lambda \sim v$ (53) for interfaces driven by a pressure (i.e., driven by a force locally normal to the interface). (*b*) A quenched disorder mechanism induced by the anisotropy of the disorder (56) or anharmonicities in the elasticity (50, 57, 77) yields a velocity independent λ. At the depinning transition only the second mechanism is relevant, but at the moment we lack a microscopic derivation and the presence of crossovers between qEW and qKPZ is still under debate.

To shed light on this puzzle, another important ingredient that should potentially be considered is the presence of defects such as bubbles and overhangs, at short length scales. The effects of these defects on the large-scale properties of the domain wall are not yet well understood. Large-scale simulations on the three-dimensional RF Ising model showed an anomalous behavior of the roughness of the interface that does not mesh with the qEW prediction (94; see also 95).

6.3. Creep Avalanches

A direct experimental access to the thermally activated events and clusters would constitute a strong test for the current theoretical picture. Repain et al. (96) observed reorganizations in the creep regime whose characteristic size qualitatively increases when lowering the field. It is not clear if these reorganizations can be identified with the thermally activated events as they look like chains of concatenated arcs (see *inset* in **Figure 14**), suggesting the presence of strong diluted

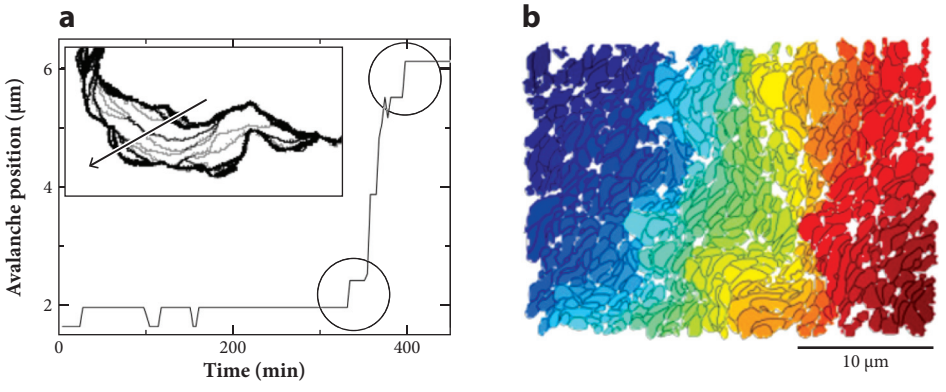

Figure 14

(*a*) Large reorganizations as obtained by Repain et al. (96) in irradiated Pt/Co/Pt thin films. The inset shows the successive domain wall configurations in a 92 × 28-μm^2 field of view. Time interval between two images is $\Delta t = 200$ s. (*b*) Sequences of magnetization reversal areas detected deep in the creep regime of Pt/Co/Pt thin films, as obtained by Grassi et al. (84). In this image time windows of $\Delta t = 15$ s were used.

pinning. More recently, Grassi et al. (84) performed a detailed and more quantitative analysis in nonirradiated Pt/Co/Pt films, focusing on regions of the sample in which strong pinning was not present. They observed almost independent thermally activated reorganizations. Their observations are consistent with the existence of creep avalanches with broad size and waiting-time distributions. It is tempting to identify them with the clusters found in numerical simulations discussed in Section 5.1.

The quantitative experimental study of creep events remains a big experimental challenge. The single thermally activated event or elementary creep event of Section 5 is systematically too small to be resolved by Kerr microscopy, even for velocities of the order of $v \sim 1$ nm/s. Partially developed clusters appear to be accessible, however, yielding indirect information about the elementary events that control the mean creep velocity. Understanding the effect of strong diluted pinning mixed with weak dense pinning is of crucial importance for a quantitative analysis, because elementary activated events could be equally associated to the collective rearrangements of typical size ℓ_{opt} or to activated depinning from strong centers.

7. CONCLUSIONS AND PERSPECTIVES

Elastic interfaces driven in disordered media represent a dramatic simplification of physical systems, such as magnetic domain walls in disordered ferromagnets. However, by encompassing the key interplay between elasticity and disorder, these models are able to predict with extraordinary precision some properties that are practically impossible to infer from more realistic microscopic approaches. An important example is provided by the creep regime. The theoretical picture is now well understood:

- The velocity versus the force characteristics displays a stretched exponential behavior.
- The geometrical properties of the interface show a crossover from an equilibrium-like behavior at short length scales to a depinning-like behavior at large length scales.
- The dynamics displays spatiotemporal patterns (creep avalanches) made of many correlated activated events. The statistical properties of these avalanches are described by the depinning critical point.

The creep regime is relevant for many physical systems, ranging from fracture fronts to contact lines or ferroelectric domain walls. The most striking confirmation comes, however, from the experiments in ferromagnetic films. There, the stretched exponential behavior of the velocity is today well established. More recently, the analysis of the MOKE images showed the fingerprints of avalanche creep dynamics.

Despite the success of the elastic interface model, many important questions remain open. First, the statistical properties of the creep avalanches are still an experimental challenge: The elementary events are too small to be resolved with MOKE microscopy, and the spatiotemporal correlations have not been characterized. Second, there is a mismatch between the roughness exponents observed in numerical simulations and those observed experimentally. Finding a solution for this puzzle is probably one of the biggest current challenges in the field. We hope these questions will motivate further research on the universal collective dynamics of elastic interfaces in random media.

DISCLOSURE STATEMENT

The authors are not aware of any affiliations, memberships, funding, or financial holdings that might be perceived as affecting the objectivity of this review.

ACKNOWLEDGMENTS

We warmly acknowledge collaborations and uncountable vivid discussions with E. Agoritsas, S. Bustingorry, N.B. Caballero, J. Curiale, G. Durin, E.A. Jagla, V. Jeudy, W. Krauth, V. Lecomte, P. Le Doussal, P. Paruch, and K. Wiese. We acknowledge the France-Argentina project ECOS-Sud No. A16E01. A.B.K. acknowledges partial support from grant number PICT2016-0069/FONCyT from Argentina and CPTGA from France for the visiting position in 2016. E.E.F. acknowledges support from grant number PICT 2017-1202/ANPCyT from Argentina. T.G. acknowledges support from the Swiss National Science foundation under Division II. This work is supported by "Investissements d'Avenir" LabEx PALM (ANR-10-LABX-0039-PALM) (EquiDystant project, L. Foini).

LITERATURE CITED

1. Barrat JL, Feigelman M, Kurchan J, Dalibard J, eds. 2003. *Slow Relaxations and Nonequilibrium Dynamics in Condensed Matter. Les Houches Session LXXVII*, July 1–26, 2002. Berlin: Springer
2. Berthier L, Biroli G. 2011. *Rev. Mod. Phys.* 83:587–645
3. Anderson PW. 1958. *Phys. Rev.* 109:1492–505
4. Evers F, Mirlin AD. 2008. *Rev. Mod. Phys.* 80:1355–417
5. Sethna JP, Dahmen KA, Myers CR. 2001. *Nature* 410:242–50
6. Baret JC, Vandembroucq D, Roux S. 2002. *Phys. Rev. Lett.* 89:195506
7. Lin J, Lerner E, Rosso A, Wyart M. 2014. *PNAS* 111:14382–87
8. Nicolas A, Ferrero EE, Martens K, Barrat JL. 2018. *Rev. Mod. Phys.* 90:045006
9. Bonamy D, Bouchaud E. 2011. *Phys. Rep.* 498:1–44
10. Schmittbuhl J, Roux S, Vilotte JP, Måløy KJ. 1995. *Phys. Rev. Lett.* 74:1787–90
11. Bonamy D, Santucci S, Ponson L. 2008. *Phys. Rev. Lett.* 101:045501
12. Ferré J, Metaxas PJ, Mougin A, Jamet JP, Gorchon J, Jeudy V. 2013. *C. R. Phys.* 14:651–66
13. Zapperi S, Cizeau P, Durin G, Stanley HE. 1998. *Phys. Rev. B* 58:6353–66
14. Paruch P, Guyonnet J. 2013. *C. R. Phys.* 14:667–84
15. Kleemann W. 2007. *Annu. Rev. Mater. Res.* 37:415–48
16. Moulinet S, Rosso A, Krauth W, Rolley E. 2004. *Phys. Rev. E* 69:035103
17. Le Doussal P, Wiese KJ, Moulinet S, Rolley E. 2009. *Europhys. Lett.* 87:56001
18. Dhar D. 1999. *Phys. A: Stat. Mech. Appl.* 263:4–25
19. Henkel M, Hinrichsen H, Lübeck S, Pleimling M. 2008. *Non-Equilibrium Phase Transitions. Vol. 1. Absorbing Phase Transitions*. Dordrecht, Neth.: Springer Sci. Bus. Media
20. Narayan O, Fisher DS. 1993. *Phys. Rev. B* 48:7030–42
21. Nattermann T, Stepanow S, Tang L-H, Leschhorn H. 1992. *J. Phys. II France* 2:1483–88
22. Fisher DS. 1998. *Phys. Rep.* 301:113–50
23. Müller M, Gorokhov DA, Blatter G. 2001. *Phys. Rev. B* 63:184305
24. Agoritsas E, Lecomte V, Giamarchi T. 2012. *Phys. B: Condens. Matter.* 407:1725–33
25. Ferrero EE, Bustingorry S, Kolton AB, Rosso A. 2013. *C. R. Phys.* 14:641–50
26. Kardar M. 1998. *Phys. Rep.* 301:85–112
27. Rosso A, Le Doussal P, Wiese KJ. 2009. *Phys. Rev. B* 80:144204
28. Kolton AB, Doussal PL, Wiese KJ. 2019. *Europhys. Lett.* 127:46001
29. Papanikolaou S, Bohn F, Sommer RL, Durin G, Zapperi S, Sethna JP. 2011. *Nat. Phys.* 7:316–20
30. Laurson L, Illa X, Santucci S, Tallakstad KT, Måløy KJ, Alava MJ. 2013. *Nat. Commun.* 4:2927
31. Scholz CH. 2002. *The Mechanics of Earthquakes and Faulting*. Cambridge, UK: Cambridge Univ. Press. 2nd ed.
32. Jagla E, Kolton A. 2010. *J. Geophys. Res.: Solid Earth* 115:B05312
33. Jagla EA, Landes FP, Rosso A. 2014. *Phys. Rev. Lett.* 112:174301
34. Janićević S, Laurson L, Måløy KJ, Santucci S, Alava MJ. 2016. *Phys. Rev. Lett.* 117:230601
35. Kolton AB, Rosso A, Giamarchi T, Krauth W. 2006. *Phys. Rev. Lett.* 97:057001

36. Fedorenko AA, Le Doussal P, Wiese KJ. 2006. *Phys. Rev. E* 74:061109
37. Ferrero EE, Bustingorry S, Kolton AB. 2013. *Phys. Rev. E* 87:032122
38. Narayan O, Fisher DS. 1992. *Phys. Rev. B* 46:11520–49
39. Le Doussal P, Wiese KJ, Chauve P. 2002. *Phys. Rev. B* 66:174201
40. Fisher DS. 1985. *Phys. Rev. B* 31:1396–427
41. Alessandro B, Beatrice C, Bertotti G, Montorsi A. 1990. *J. Appl. Phys.* 68:2908–15
42. Doussal PL, Vinokur VM. 1995. *Phys. C: Supercondens.* 254:63–68
43. Joanny J, De Gennes PG. 1984. *J. Chem. Phys.* 81:552–62
44. Gao H, Rice JR. 1989. *J. Appl. Mech.* 56:828–36
45. Kolton AB, Jagla EA. 2018. *Phys. Rev. E* 98:042111
46. Chauve P, Giamarchi T, Le Doussal P. 2000. *Phys. Rev. B* 62:6241–67
47. Le Doussal P, Wiese KJ. 2013. *Phys. Rev. E* 88:022106
48. Le Priol C, Chopin J, Le Doussal P, Ponson L, Rosso A. 2020. *Phys. Rev. Lett.* 124:065501
49. Rosso A, Krauth W. 2002. *Phys. Rev. E* 65:025101
50. Rosso A, Hartmann AK, Krauth W. 2003. *Phys. Rev. E* 67:021602
51. Ramanathan S, Fisher DS. 1998. *Phys. Rev. B* 58:6026–46
52. Leschhorn H. 1993. *Phys. A: Stat. Mech. Appl.* 195:324–35
53. Kardar M, Parisi G, Zhang YC. 1986. *Phys. Rev. Lett.* 56:889–92
54. Middleton AA. 1995. *Phys. Rev. E* 52:R3337–40
55. Zoia A, Rosso A, Kardar M. 2007. *Phys. Rev. E* 76:021116
56. Tang LH, Kardar M, Dhar D. 1995. *Phys. Rev. Lett.* 74:920–23
57. Rosso A, Krauth W. 2001. *Phys. Rev. Lett.* 87:187002
58. Buldyrev SV, Havlin S, Stanley HE. 1993. *Phys. A: Stat. Mech. Appl.* 200:200–11
59. Tang LH, Leschhorn H. 1992. *Phys. Rev. A* 45:R8309–12
60. Jeong H, Kahng B, Kim D. 1996. *Phys. Rev. Lett.* 77:5094–97
61. Atis S, Dubey AK, Salin D, Talon L, Le Doussal P, Wiese KJ. 2015. *Phys. Rev. Lett.* 114:234502
62. Lemerle S, Ferré J, Chappert C, Mathet V, Giamarchi T, Le Doussal P. 1998. *Phys. Rev. Lett.* 80:849–52
63. Kim KJ, Lee JC, Ahn SM, Lee KS, Lee CW, et al. 2009. *Nature* 458:740–42
64. Jeudy V, Mougin A, Bustingorry S, Savero Torres W, Gorchon J, et al. 2016. *Phys. Rev. Lett.* 117:057201
65. Ioffe LB, Vinokur VM. 1987. *J. Phys. C: Solid State Phys.* 20:6149–58
66. Nattermann T. 1987. *Europhys. Lett.* 4:1241–46
67. Vinokur VM, Marchetti MC, Chen LW. 1996. *Phys. Rev. Lett.* 77:1845–48
68. Anderson PW, Kim YB. 1964. *Rev. Mod. Phys.* 36:39–43
69. Agoritsas E, García-García R, Lecomte V, Truskinovsky L, Vandembroucq D. 2016. *J. Stat. Phys.* 164:1394–428
70. Kolton AB, Rosso A, Giamarchi T, Krauth W. 2009. *Phys. Rev. B* 79:184207
71. Drossel B, Kardar M. 1995. *Phys. Rev. E* 52:4841–52
72. Kolton AB, Rosso A, Giamarchi T. 2005. *Phys. Rev. Lett.* 94:047002
73. Rosso A, Krauth W. 2001. *Phys. Rev. B* 65:012202
74. Ferrero EE, Foini L, Giamarchi T, Kolton AB, Rosso A. 2017. *Phys. Rev. Lett.* 118:147208
75. Arcangelis L, Godano C, Grasso JR, Lippiello E. 2016. *Phys. Rep.* 628:1–91
76. Purrello VH, Iguain JL, Kolton AB, Jagla EA. 2017. *Phys. Rev. E* 96:022112
77. Purrello VH, Iguain JL, Kolton AB. 2019. *Phys. Rev. E* 99:032105
78. Gorchon J, Bustingorry S, Ferré J, Jeudy V, Kolton AB, Giamarchi T. 2014. *Phys. Rev. Lett.* 113:027205
79. Cao X, Bouzat S, Kolton AB, Rosso A. 2018. *Phys. Rev. E* 97:022118
80. Diaz Pardo R, Savero Torres W, Kolton AB, Bustingorry S, Jeudy V. 2017. *Phys. Rev. B* 95:184434
81. Caballero NB, Fernández Aguirre I, Albornoz LJ, Kolton AB, Rojas-Sánchez JC, et al. 2017. *Phys. Rev. B* 96:224422
82. Caballero NB, Ferrero EE, Kolton AB, Curiale J, Jeudy V, Bustingorry S. 2018. *Phys. Rev. E* 97:062122
83. Jeudy V, Díaz Pardo R, Savero Torres W, Bustingorry S, Kolton AB. 2018. *Phys. Rev. B* 98:054406
84. Grassi MP, Kolton AB, Jeudy V, Mougin A, Bustingorry S, Curiale J. 2018. *Phys. Rev. B* 98:224201
85. Herrera Diez L, Jeudy V, Durin G, Casiraghi A, Liu YT, et al. 2018. *Phys. Rev. B* 98:054417

86. Domenichini P, Quinteros CP, Granada M, Collin S, George JM, et al. 2019. *Phys. Rev. B* 99:214401
87. Shahbazi K, Kim JV, Nembach HT, Shaw JM, Bischof A, et al. 2019. *Phys. Rev. B* 99:094409
88. Larkin AI, Ovchinnikov YN. 1979. *J. Low Temp. Phys.* 34:409–28
89. Nattermann T, Shapir Y, Vilfan I. 1990. *Phys. Rev. B* 42:8577–86
90. Démery V, Lecomte V, Rosso A. 2014. *J. Stat. Mech.: Theory Exp.* 2014:P03009
91. Shibauchi T, Krusin-Elbaum L, Vinokur VM, Argyle B, Weller D, Terris BD. 2001. *Phys. Rev. Lett.* 87:267201
92. Moon KW, Kim DH, Yoo SC, Cho CG, Hwang S, et al. 2013. *Phys. Rev. Lett.* 110:107203
93. Diaz Pardo R, Moisan N, Albornoz L, Lemaitre A, Curiale J, Jeudy V. 2019. *Phys. Rev. B* 100:184420
94. Clemmer JT, Robbins MO. 2019. *Phys. Rev. E* 100:042121
95. Zhou NJ, Zheng B. 2014. *Phys. Rev. E* 90:012104
96. Repain V, Bauer M, Jamet J-P, Ferré J, Mougin A, et al. 2004. *Europhys. Lett.* 68:460–66

Annual Review of Condensed Matter Physics

Volume 12, 2021

Contents

Errata

An online log of corrections to *Annual Review of Condensed Matter Physics* articles may be found at http://www.annualreviews.org/errata/conmatphys